Supporting Information

Combined catalyst-pathway design for efficient and green urea synthesis

Zhuohang Li, Xuezi Xing, Ruichao Zhang, Xue Zeng*, Ke Chu*
School of Materials Science and Engineering, Lanzhou Jiaotong University, Lanzhou 730070, China
*Corresponding author. E-mail: zengxue@lzjtu.edu.cn (X. Zeng), chuk630@mail.lzjtu.cn (K. Chu)

Experimental Section

Materials

All the reagents were of analytical grade and were used as received without further purification. TiO_2 (≥99.9%), $AgNO_3$ (≥99.0%), $C_4H_6N_2$ (≥99.9%), CH_4O (≥99.9%), NaOH (≥96.0%), $C_7H_6O_3$ (≥99.5%), KOH (≥99.9%), $KHCO_3$ (≥99.9%), NH_4Cl (≥99.5%), $C_6H_5Na_3O_7 \cdot 2H_2O$ (≥99.0%), $C_5FeN_6Na_2O \cdot 2H_2O$ (≥99.0%), urease, NaClO (≥99.9%) and Nafion (5 wt%) were provided from Sigma-Aldrich Chemical Reagent Co, Ltd. H_2SO_4 (98%), $N_2H_4 \cdot H_2O$ (≥99.9%) and C_2H_5OH (99.0%) were purchased from Sigma-Aldrich Chemical Reagent Co, Ltd. CO_2 (≥99.999%) and Ar (≥99.999%) are provided from Lanzhou Xinwanke, Co, Ltd.

Synthesis of Ag_1/TiO_{2-x}

All the chemicals were used as received without further purification. 2 g of pure TiO_2 powder was dispersed in 40 mL of 5 M NaOH solution under stirring for 1 h. The suspension was then hydrothermally treated in a Teflon-lined autoclave at 180 °C for 24 h. After cooling, the precipitates were collected, dried and further annealed in Ar atmosphere at 500 °C for 2 h. The obtained TiO_{2-x} was re-dispersed in an aqueous solution containing dissolved $AgNO_3$ and maintained for 2 h. The resulting sediments were then collected, washed thoroughly and dried to obtain Ag_1/TiO_{2-x}.

Electrochemical experiments in H-type cell

Electrochemical measurements were conducted utilizing a CHI-760E electrochemical workstation. The experimental setup comprised a three-electrode cell configuration, consisting of an Ag_1/TiO_{2-x} working electrode, an Ag/AgCl reference electrode, and a Pt foil counter electrode. The catalyst slurry was prepared by dissolving 25 mg of catalyst in 3 mL of isopropanol followed by the addition of 20 μL of Nafion ionomer solution (5 wt% H_2O solution). The catalyst slurry was slowly dripped onto carbon paper (Sigracet 29 BC) to obtain ~0.5 mg cm^{-2} of catalyst loading as electrode. All potentials were calibrated with respect to a reversible hydrogen electrode (RHE) using the formula E (V vs. RHE) = E (V vs. Ag/AgCl) + 0.198 V + 0.059 × pH. The catholyte was a solution containing gases generated through plasma

and 0.1 M $KHCO_3$, while the anolyte consisted of a 1 M KOH solution within an H-type two-compartment electrochemical cell separated by a Nafion 211 membrane. Before utilizing the Nafion membrane, a pretreatment procedure was carried out. The membrane was heated in a 5% H_2O_2 aqueous solution at 80°C for 1 h, followed by rinsing with deionized water at 80°C for an additional 1 h. The catholyte was purged with CO_2 or Ar prior to the electrochemical experiments. After electrolysis for 1 h, the produced urea was quantitatively determined by the urease decomposition method.

Electrochemical experiments in flow cell

Flow cell measurements were conducted using a commercially available flow cell electrolyser (101017, Gaoss Union Technology Co, LTD). In flow cell, the anodic and cathodic chambers were separated by a Nafion 211 proton exchange membrane (PEM). For the electrochemical measurements, a gas diffusion electrode (GDE) was used as the working electrode, Ni foams served as the counter electrode, and an Ag/AgCl electrode was employed as the reference electrode. During the electrolysis, CO_2 gas was fed from the no-catalyst side of the GDE at a flow rate of 20 s.c.c.m., and both catholyte and anolyte were continuously cycled at a rate of 20 mL min^{-1} under pump drive. After electrolysis at specified potentials for 1 h, the produced urea was quantitatively determined by the urease decomposition method.

Plasma-assisted air-to-NO_x^- conversion

A pulsed high-voltage plasma discharge (PHPD) system was employed to activate and dissociate air molecules for NO_x generation. The system primarily comprised three key components: power regulation module, plasma reactor and gas flow control system. The power regulation module was powered by a low-voltage direct current (DC) power supply and integrated with a high-voltage module (Model: DC High-Voltage Modules-150KV, Guangao Technology (Wuhan) Co., Ltd) to amplify the voltage. The output potential was precisely measured using a high-voltage voltmeter (Model: 69C17, Wenzhou Telun Electric Co., Ltd). The plasma reactor comprised a glass tube (2 mm in inner diameter), two copper electrodes with multiple parallel microcolumns, along with a gas inlet and outlet for feeding and discharging gases, respectively. Ambient air was directly introduced into the plasma reactor at a

controlled volumetric flow rate regulated by a gas flow control system (Model: ACU10FD-XS, Beijing Precision Technology Co., Ltd). After a period of plasma discharge, the outlet NO_x gas was absorbed in an Erlenmeyer flask containing 1 M KOH solution, where NO_x was converted into NO_x ions (NO_2^-/NO_3^-). The resulting NO_2^- and NO_3^- concentrations were subsequently quantified with ultraviolet-visible (UV-Vis) absorption spectroscopy.

Characterizations

X-ray diffraction (XRD) pattern was collected on a Rigaku D/max 2400 diffractometer with Cu Kα radiation (λ =1.5418 Å, 40 kV). Transmission electron microscopy (TEM) and high-resolution transmission electron microscopy (HRTEM) were recorded on a Tecnai G^2 F20 microscope. Aberration-corrected high-angle annular dark-field scanning transmission microscopy (AC-STEM) was performed on a Titan Cubed Themis G^2 300 microscope. Electron paramagnetic resonance (EPR) measurements were conducted on a Bruker ESP-300 spectrometer. Operando Raman spectroscopy analysis was carried out on a confocal Raman spectrometer (Horiba HR-800) with a wavelength of 532 nm. Operando Fourier-transform infrared (FTIR) spectroscopy was performed on a Nicolet 6700 FTIR spectrometer. Online differential electrochemical mass spectrometry (DEMS, QAS 100) was performed by QAS 100 spectrometer.

Determination of urea

Urea concentration was detected via urease decomposition method[1]. Typically, 0.2 mL of urease solution with concentration of 5 mg mL^{-1} was added into 2 mL of urea electrolyte, and then reacted at 37℃ in constant temperature shaker for 40 min. Urea was decomposed by urease into CO_2 and two NH_3 molecules. After the decomposition, NH_3 concentration of urea electrolyte with urease (c_{urease}) was detected via above indophenol blue method. Meanwhile, NH_3 concentration contained in urea electrolyte without urease (c_{NH3}) was also quantified by indophenol blue

method. Urea concentration (c_{urea}) in electrolyte were calculated by the following equation:

$$c_{urea} = (c_{urease} - c_{NH3})/2 \quad (1)$$

The urea yield rate and FE_{urea} were calculated by the following equation:

$$\text{Urea yield rate}\,(mmol\ h^{-1}\ g^{-1}) = \frac{c_{urea} \times V}{60.06 \times t \times m} \quad (2)$$

$$FE_{urea}\,(\%) = \frac{12 \times F \times c_{urea} \times V}{60.06 \times Q} \times 100\% \quad (3)$$

where c_{urea} (mg mL^{-1}) is the measured urea concentration, V (mL) is the volume of the electrolyte, t (h) is the reduction time, m (g) is the mass loading of the catalyst on CC, F (96500 C mol^{-1}) is the Faraday constant, Q (C) is the quantity of applied electricity.

Determination of NH_3

NH_3 in electrolyte was quantitatively determined by the indophenol blue method[2]. Typically, 2 mL of electrolyte was removed from the electrochemical reaction vessel and diluted with deionized water. Then 2 mL of diluted solution was removed into a clean vessel followed by sequentially adding NaOH solution (2 mL, 1 M) containing $C_7H_6O_3$ (5 wt.%) and $C_6H_5Na_3O_7$ (5 wt.%), NaClO (1 mL, 0.05 M), and $C_5FeN_6Na_2O$ (0.2 mL, 1wt.%) aqueous solution. After the incubation for 2 h at room temperature, the mixed solution was subjected to UV-vis measurement using the absorbance at 655 nm wavelength. The concentration-absorbance curves were calibrated by the standard NH_4Cl solution with a series of concentrations.

Determination of NO_2^-

NO_2^- in electrolyte was determined by a Griess test[3]. Typically, 2 mL of electrolyte was removed from the electrochemical reaction vessel and diluted with deionized water. The coloring solution was prepared by dissolving N-(1-naphthyl) ethylenediamine dihydrochloride (0.1 g), sulfonamide (1.0 g) and H_3PO_4 (2.94 mL, 85%) into 50 mL of deionized water. Add 0.1 mL of coloring solution to the diluted electrolyte. After incubation for 30 min at room temperature, the mixture was

subjected to UV-vis measurements and the absorption spectrum (range 400-700 nm) was obtained. The absorbance at 540 nm was measured to determine the concentration of generated NO_2^- with a standard curve of $NaNO_2$.

Determination of NO_3^-

NO_3^- in electrolyte was quantitatively determined by a reported method[4]. The electrolyte was collected and diluted to the detection range. 2 mL of diluted electrolyte was mixed with 40 μL of 1.0 M HCl containing 4.0 μL of 0.8 wt% sulfamic acid. After the incubation for 20 min at room temperature, the mixed solution was subjected to UV-vis measurement using the absorbance at 220 nm wavelength. The concentration-absorbance curves were calibrated by the standard KNO_3 solution with a series of concentrations.

Calculation details

DFT calculations were carried out using the Cambridge sequential total energy package (CASTEP) with ultrasoft pseudopotentials. The exchange-correlation functional is evaluated using the Perdew-Burke-Ernzerhof (PBE) in the generalized gradient approximation. DFT-D3 method was employed to calculate the van der Waals (vdW) interactions. According to the experimental characterizations, the Ag_1/TiO_{2-x} (101) slab was modeled and a vacuum region of 15 Å. A vacuum region of 15 Å was used to separate adjacent slabs. The cutoff energy was set as 450 eV and the k-point meshes were set as 2 × 2 × 1. The AIMD simulation was carried out to estimate the thermal stability, in which the NVT ensemble is chosen with the total simulation time of 5 ns at a time step of 1 fs.

The computational hydrogen electrode (CHE) model was adopted to calculate the Gibbs free energy change (ΔG) for each elementary step as follows:

$$\Delta G = \Delta E + \Delta E_{ZPE} - T\Delta S \quad (4)$$

where ΔE represents the electronic energy contribution directly derived from DFT calculations. ΔEZPE and $T\Delta S$ denote the contributions of zero-point energy and

entropy (at 298.15 K), respectively. These values can be obtained from the NIST database for free molecules[5].

Molecular dynamics (MD) simulations were performed using the Forcite module. The electrolyte system was modeled by a cubic cell with placing catalyst at the center of the cell and randomly filling 1000 H_2O, 50 NO_2^-, 50 CO_2 molecules, and 50 H atoms. The force field type was chosen as universal. After geometry optimization, the MD simulations were performed in an NVT ensemble (698 K) with the total simulation time of 5 ns at a time step of 1 fs.

The radial distribution function (RDF) is calculated by[6]:

$$g(r) = \frac{dN}{4\pi\rho r^2 dr} \tag{5}$$

where dN is the amount of molecules in the shell between the central particle r and $r+dr$, ρ is the number density of NO_2^-, CO_2, H_2O and H.

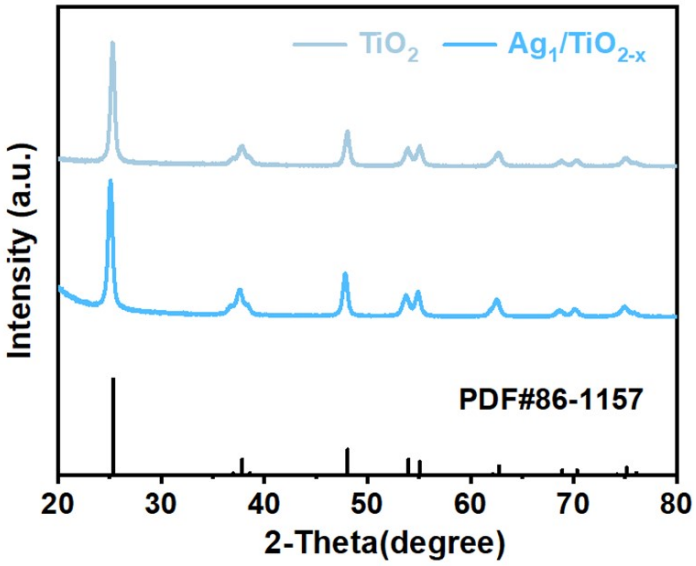

Fig. S1. XRD patterns of Ag_1/TiO_{2-x} and TiO_2.

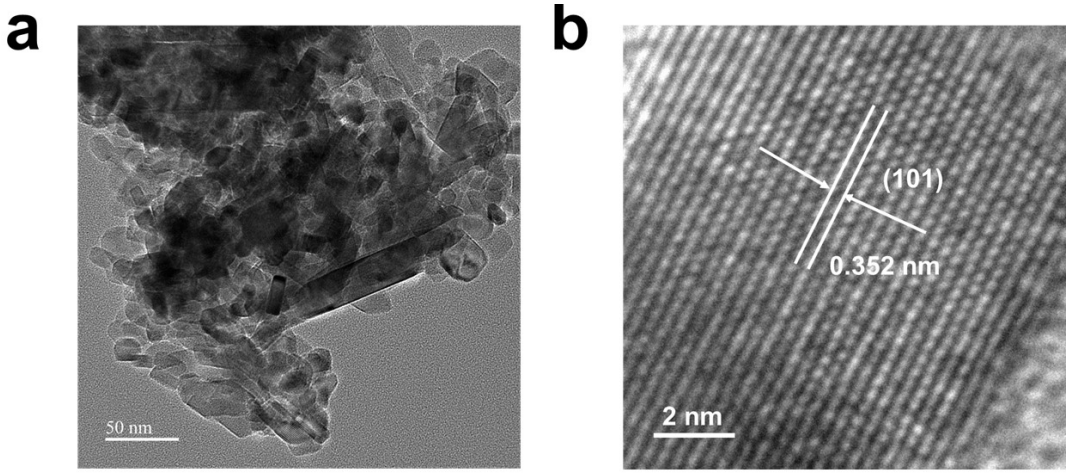

Fig. S2. (a) TEM and (b) HRTEM images of Ag_1/TiO_{2-x}.

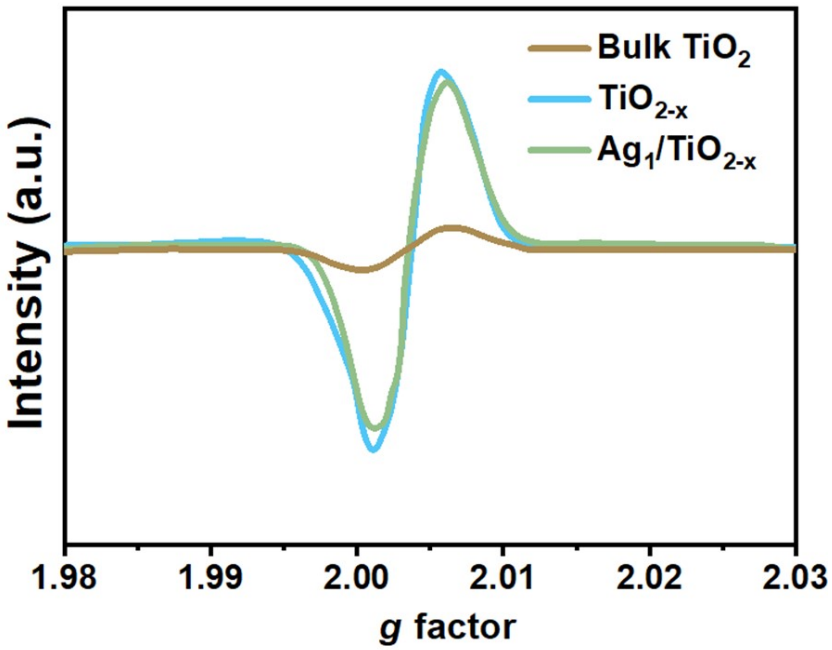

Fig. S3. EPR spectra of bulk TiO_2, TiO_{2-x} and Ag_1/TiO_{2-x}.

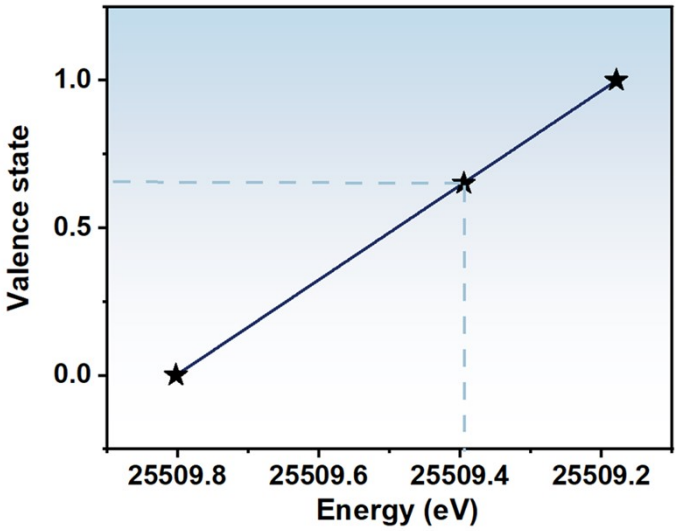

Fig. S4. XANES fitted average Ag valence state of Ag_1/TiO_{2-x}.

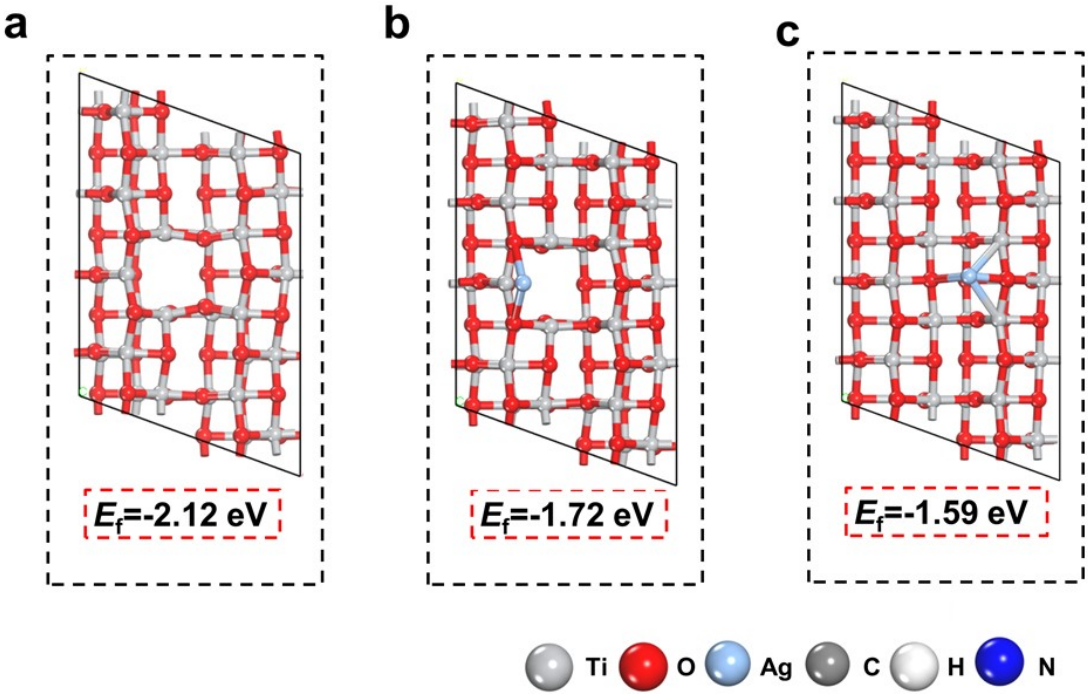

Fig. S5. Calculated formation energies (E_f) of (a) TiO_{2-x}, (b) Ag_1/TiO_{2-x} and (b) Ag_1/TiO_2.

The calculated formation energies (E_f) indicate that OV can be energetically favorable formed on TiO_2 to form TiO_{2-x} (Fig. S5a), and Ag_1 can be well anchored onto OV to generate Ag_1/TiO_{2-x} catalyst (Fig. S5b).

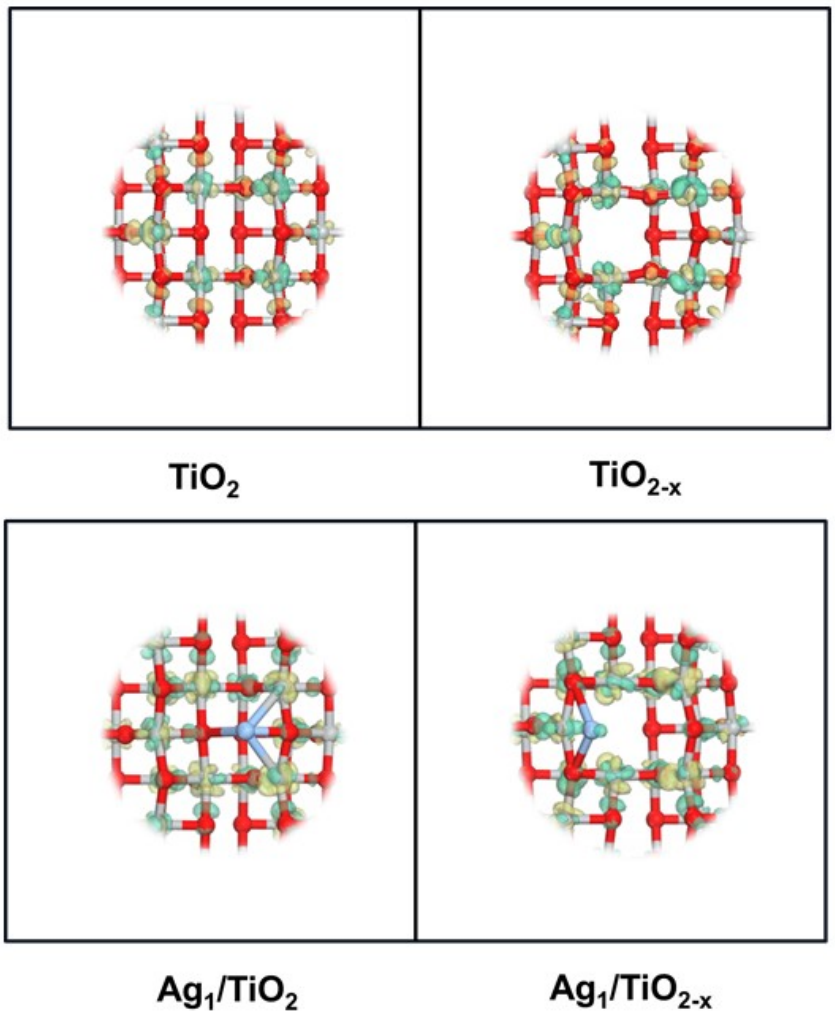

Fig. S6. Differential charge density maps of TiO_2, TiO_{2-x}, Ag_1/TiO_2 and Ag_1/TiO_{2-x} (Yellow: accumulation and cyan: depletion).

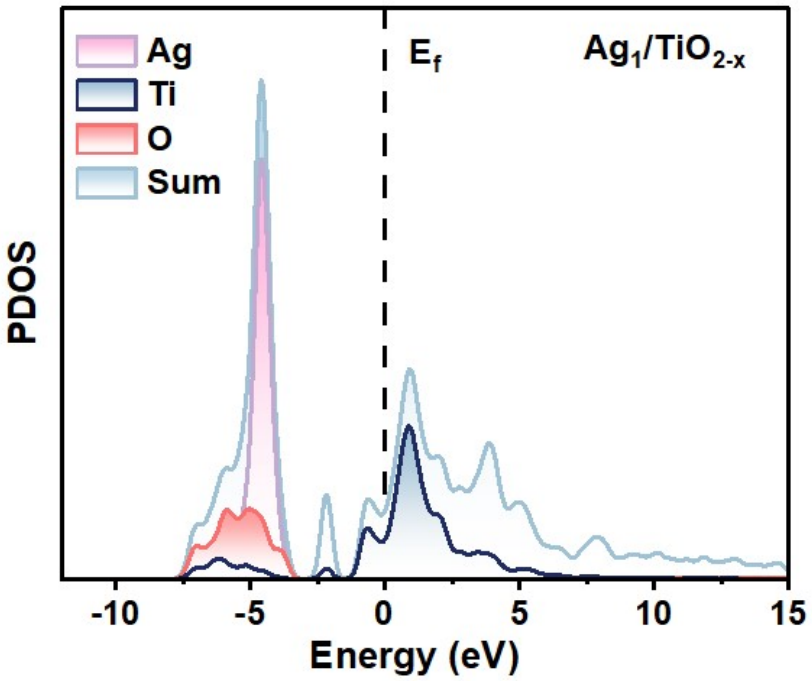

Fig. S7. PDOS profile of Ag_1/TiO_{2-x}.

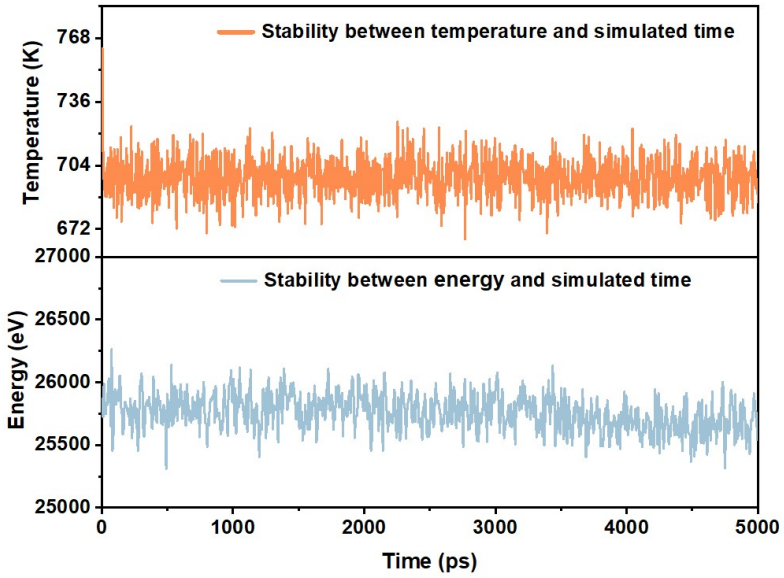

Fig. S8. AIMD simulation of the Ag_1/TiO_{2-x} atomic structure. The AIMD simulation was carried out to estimate the thermal stability, in which the NVT ensemble is chosen with the total simulation time of 5 ns at a time step of 1 fs.

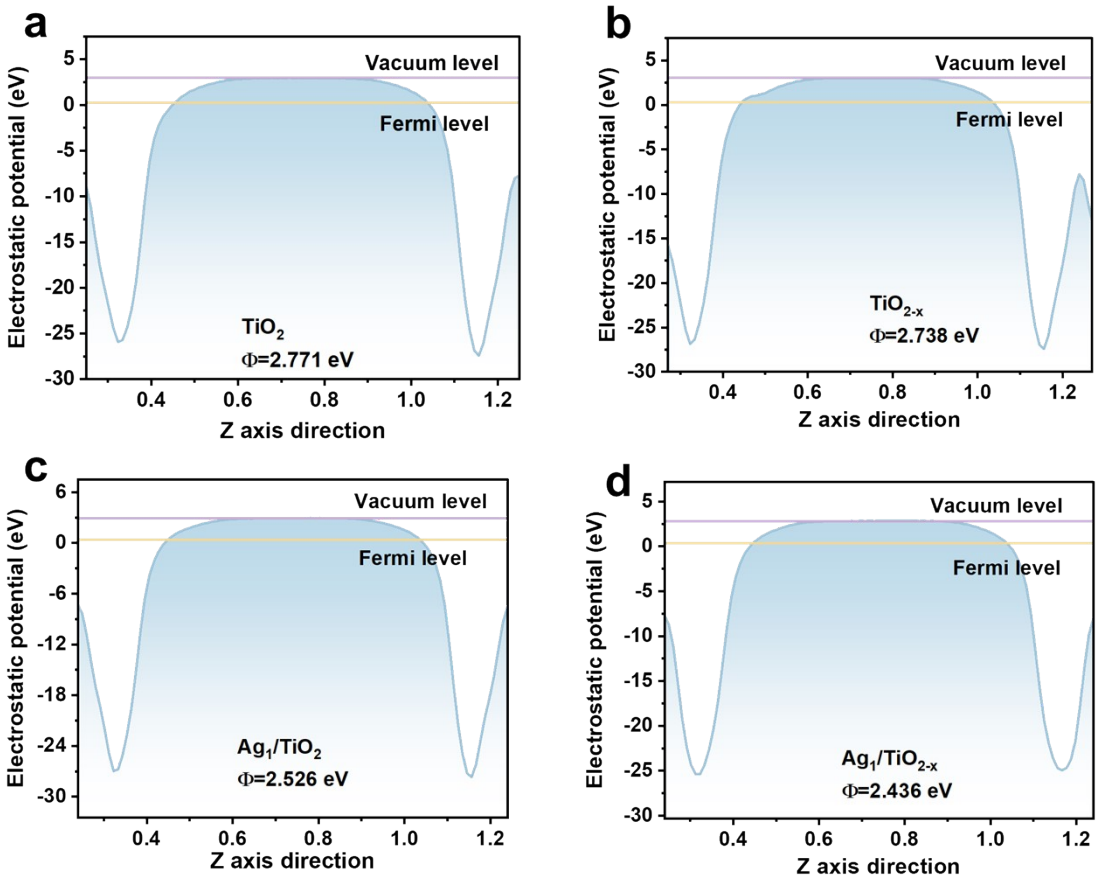

Fig. S9. Average potential profiles along c-axis direction for calculating the work functions of (a) TiO_2, (b) TiO_{2-x}, (c) Ag_1/TiO_2 and (d) Ag_1/TiO_{2-x}.

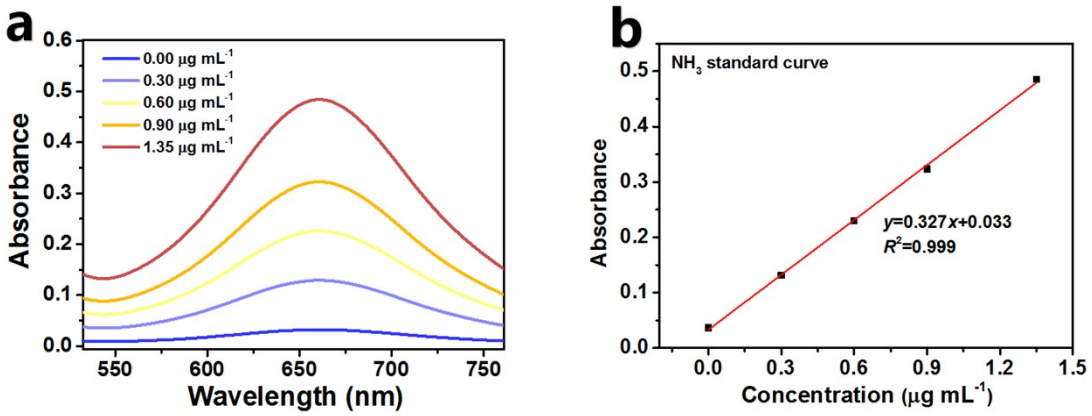

Fig S10. (a) UV-vis absorption spectra of NH_4Cl assays after incubated for 2 h at ambient conditions. (b) Calibration curve used for the calculation of NH_3 concentrations.

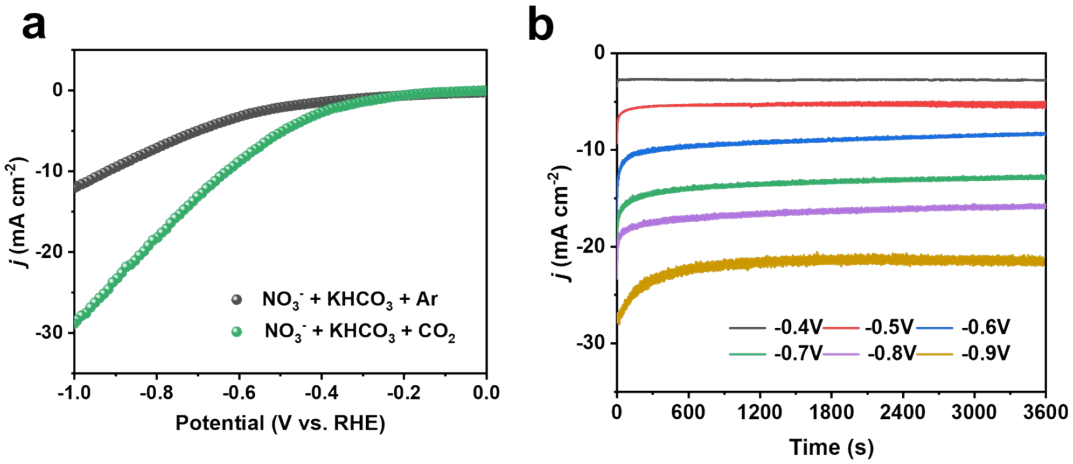

Fig S11. (a) LSV curves of Ag_1/TiO_{2-x} during the UECN electrolysis in H-cell. (b) Chronoamperometry curves at different potentials of Ag_1/TiO_{2-x} in H-cell.

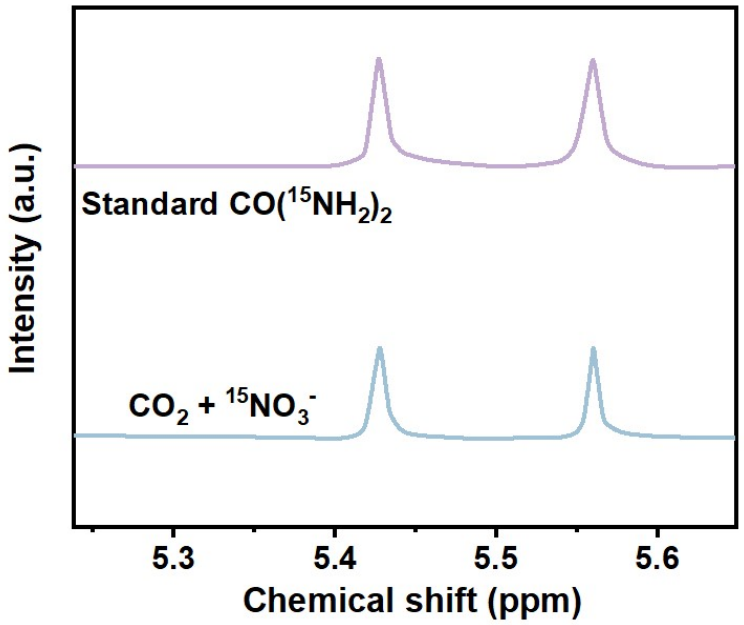

Fig. S12. ^{1}H NMR spectra of $CO(^{15}NH_2)_2$ standard sample and those electrolyzed in $^{15}NO_3^-$ electrolyte at -0.7 V.

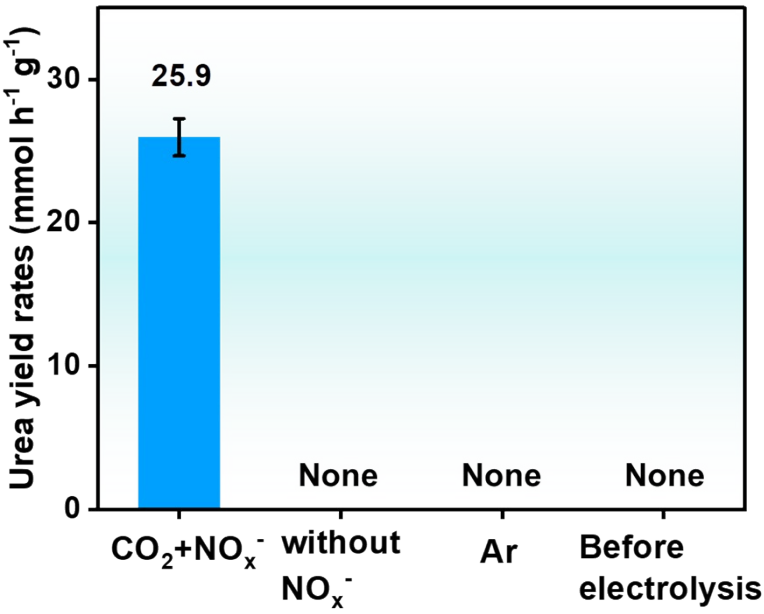

Fig. S13. Amounts of produced urea on Ag_1/TiO_{2-x} under different conditions: (1) electrolysis in NO_x^- +CO_2^- solution, (2) without NO_x^-, (3) without CO_2, (4) before electrolysis.

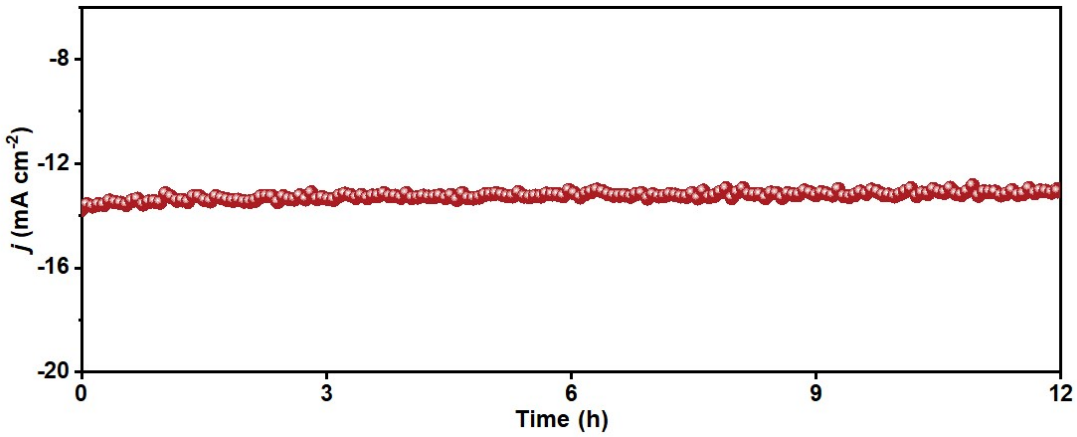

Fig. S14. Long-term test of Ag_1/TiO_{2-x} in H-cell at -0.7 V.

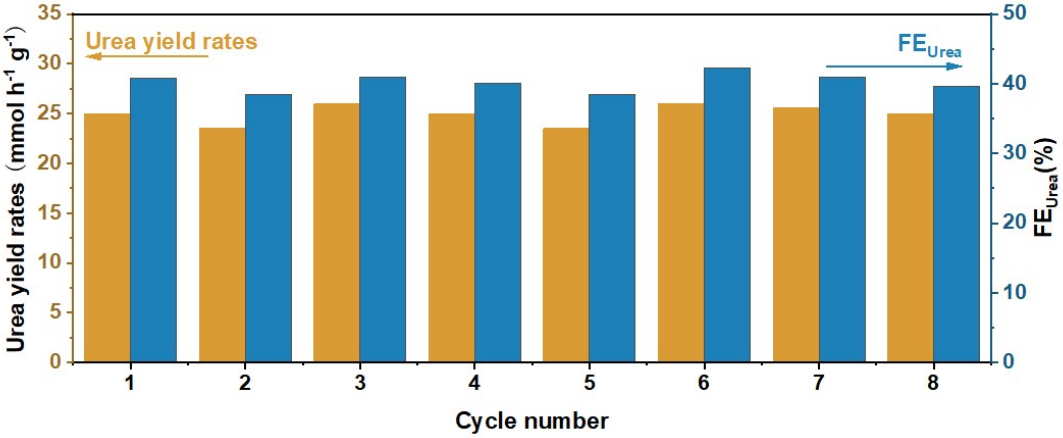

Fig. S15. Cycling test of Ag_1/TiO_{2-x} in H-cell at -0.7 V.

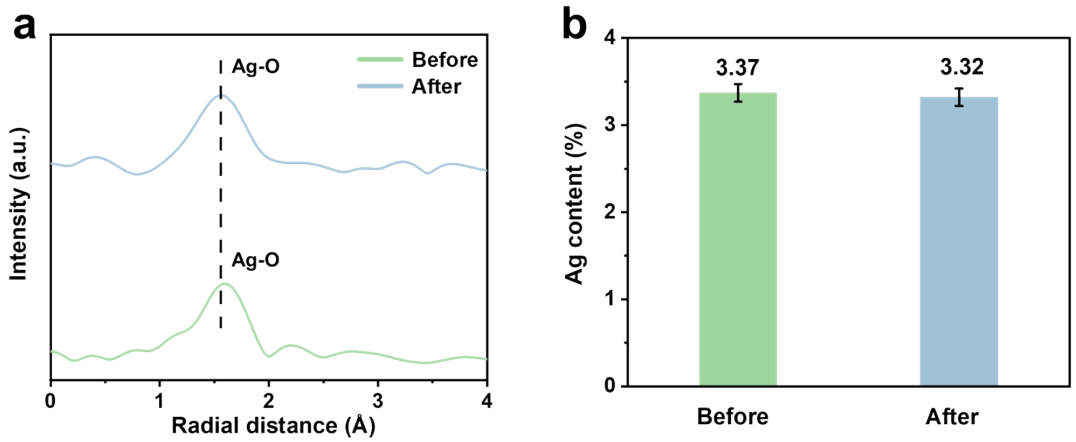

Fig. S16. (a) EXAFS spectra and (b) ICP analyses of Ag_1/TiO_{2-x} before and after long-term electrolysis test.

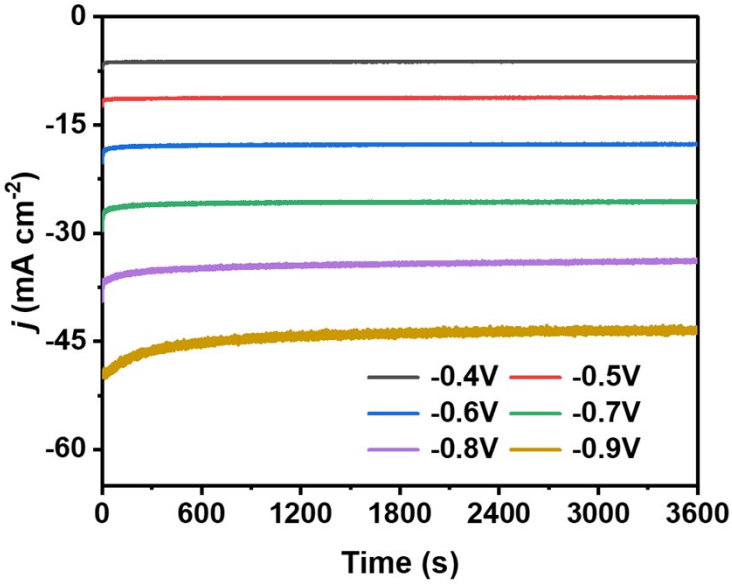

Fig. S17. Potential-dependent chronoamperometry curves of Ag_1/TiO_{2-x} after 1 h electrolysis in flow cell.

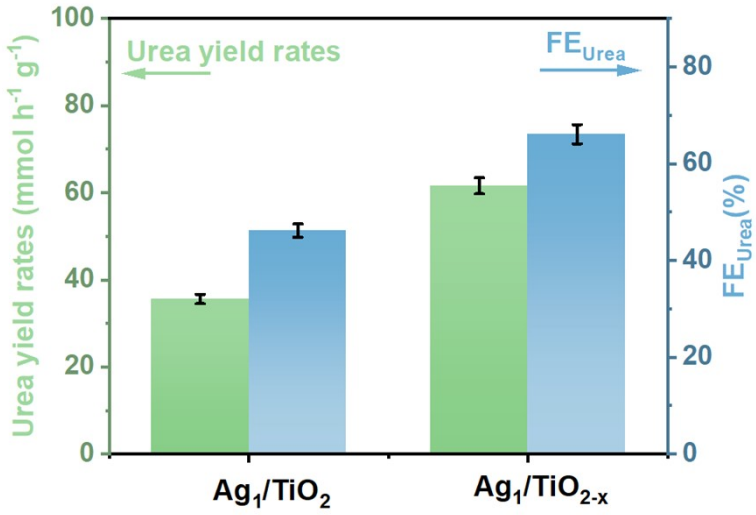

Fig. S18. UECN performance comparison between Ag_1/TiO_2 and Ag_1/TiO_{2-x} after electrolysis for 1 h in flow cell.

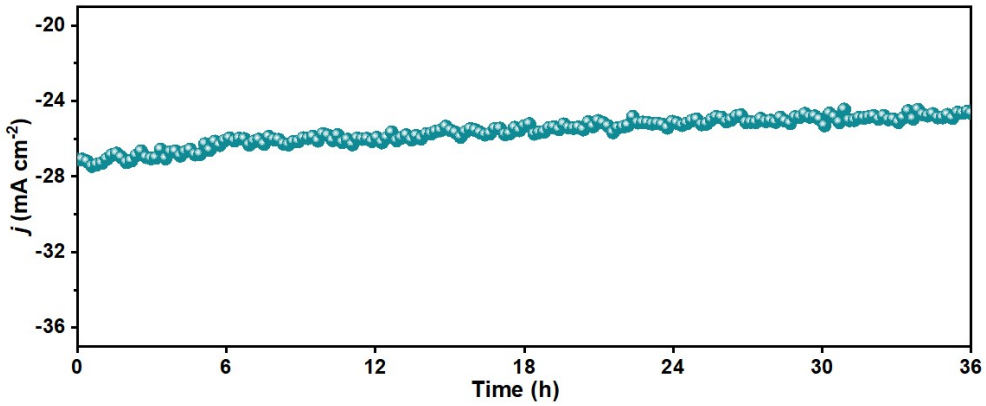

Fig. S19. Long-term test of Ag_1/TiO_{2-x} in flow-cell at -0.7 V.

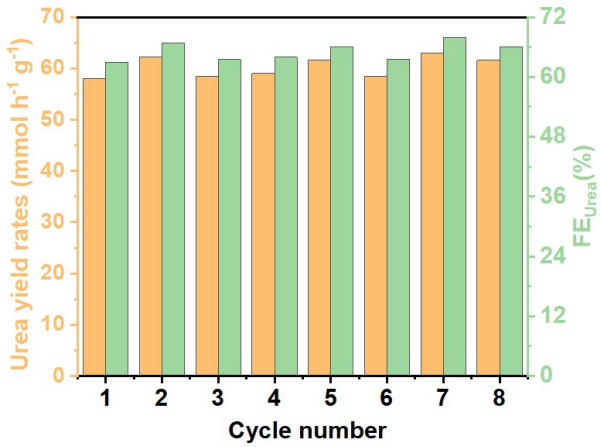

Fig. S20. Cycling test of Ag_1/TiO_{2-x} in flow cell at -0.7 V.

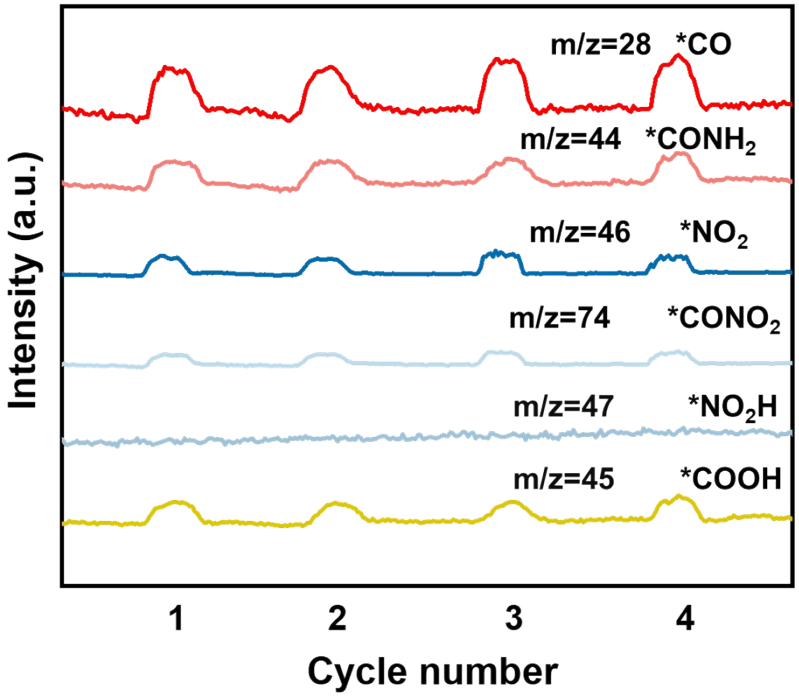

Fig. S21. Online DEMS spectra of Ag_1/TiO_{2-x} during the UECN electrolysis at -0.7 V.

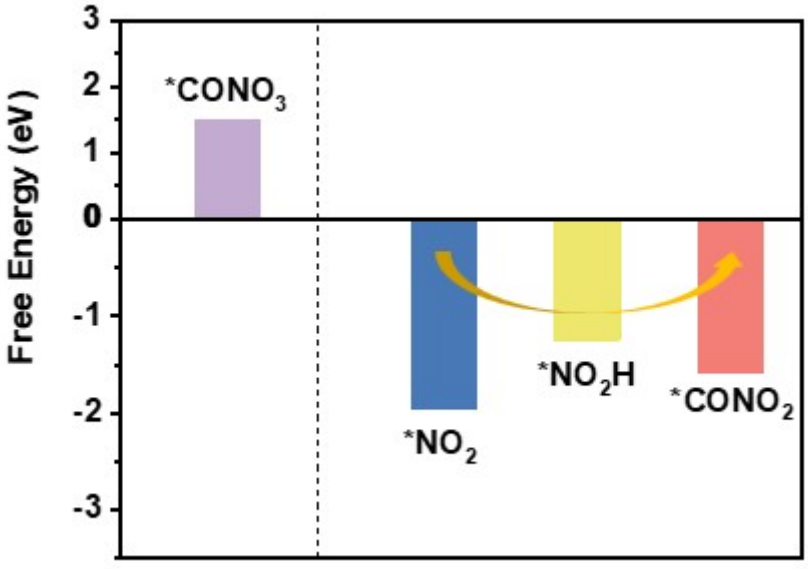

Fig. S22. Free energy diagrams of various potential N-intermediates.

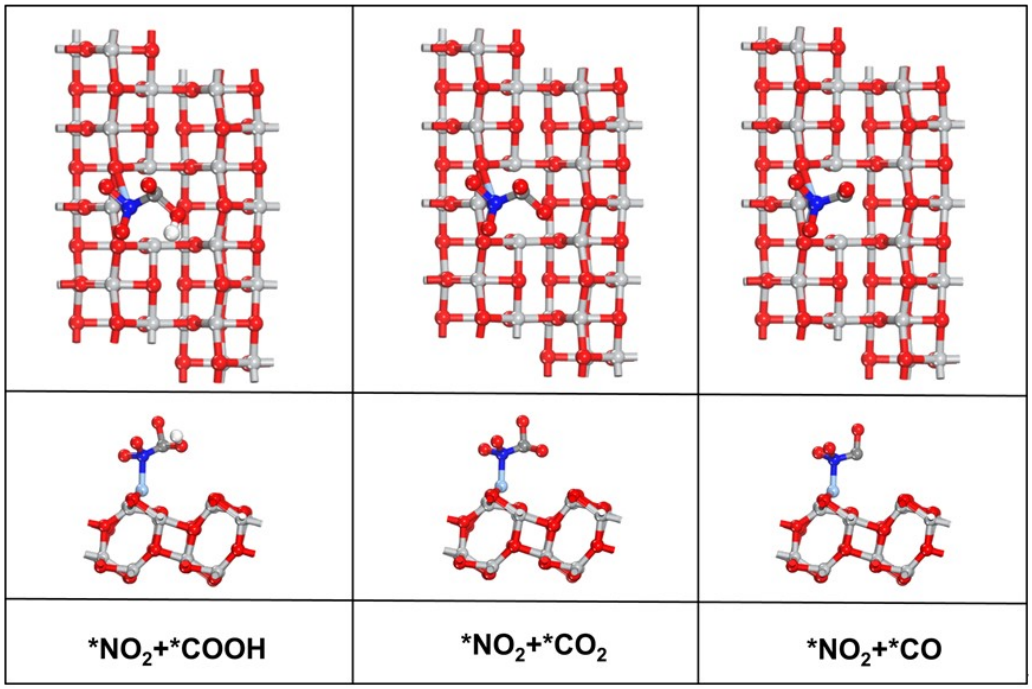

Fig. S23. Optimized structures of the coupling of $*NO_2$ with various C-intermediates.

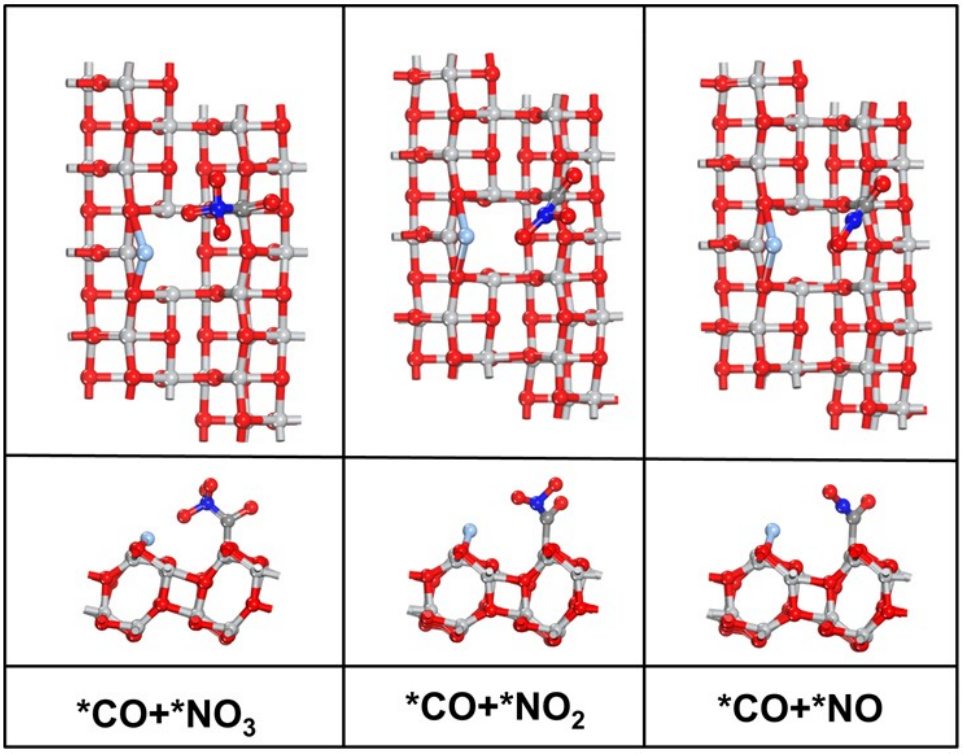

Fig. S24. Optimized structures of the coupling of *CO with various N-intermediates.

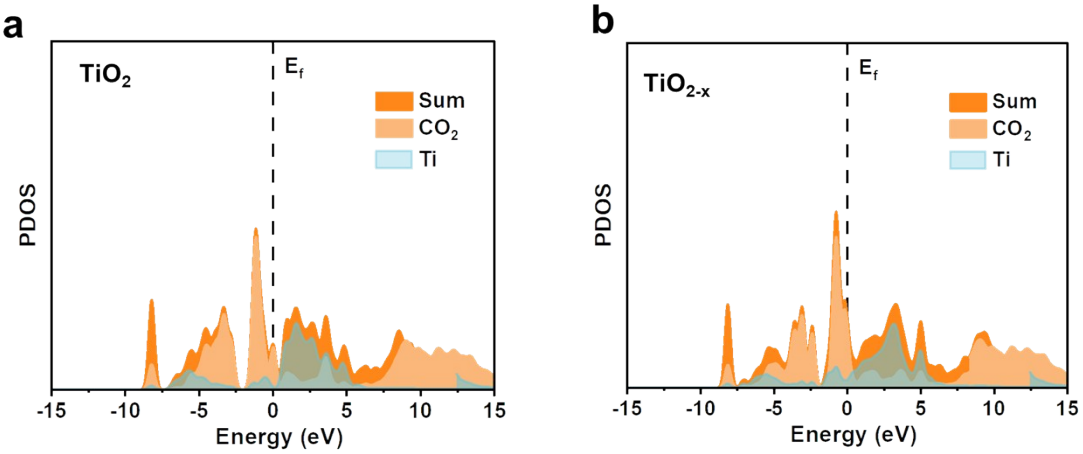

Fig. S25. PDOS profiles of adsorbed CO_2 on (a) TiO_2 and (b) TiO_{2-x}.

PDOS map shows pronounced Ti_{OV}/*CO_2 electronic interaction where Ti_{OV} can effectively donate electrons into the unoccupied orbitals of *CO_2, facilitating its activation and C=O bond cleavage.

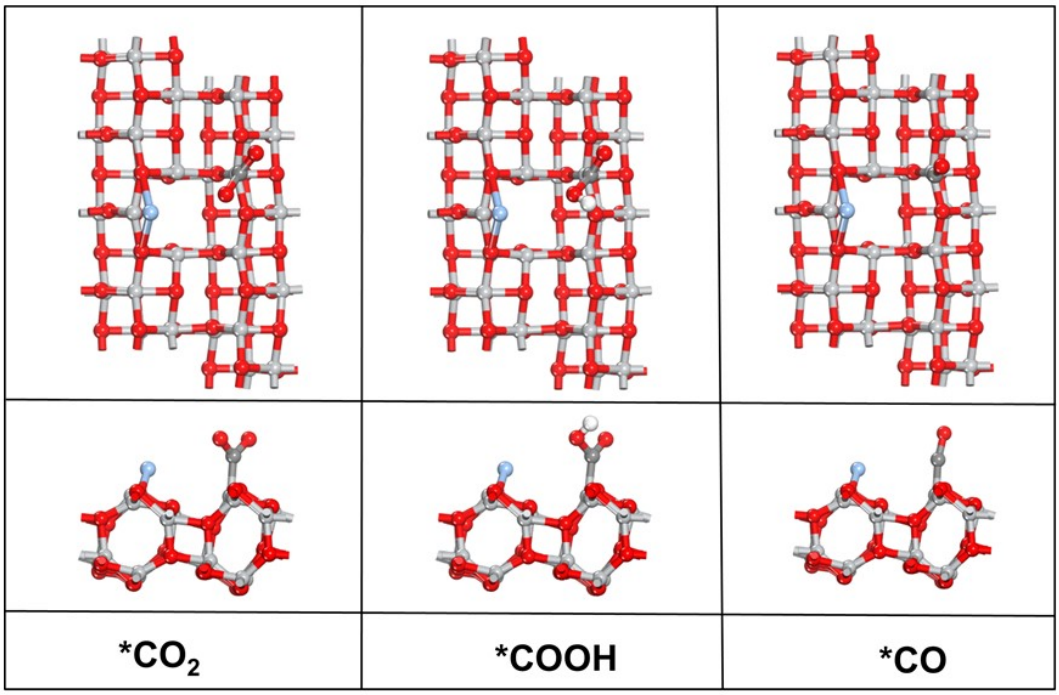

Fig. S26. Optimized structures of the reaction intermediates on Ag_1/TiO_{2-x} along $CO_2 \rightarrow$*CO pathway.

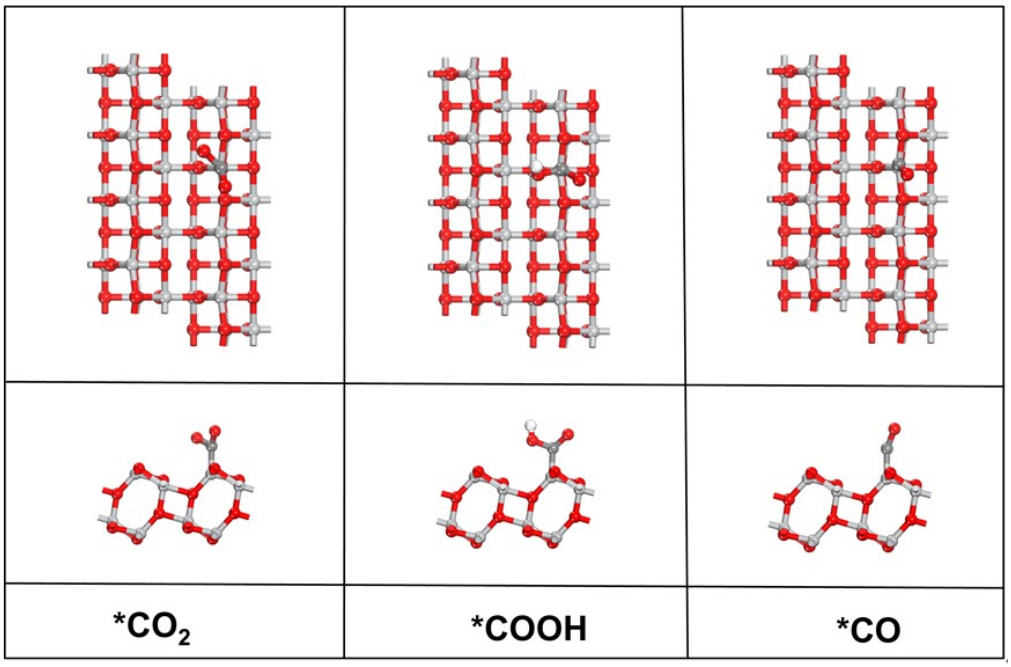

Fig. S27. Optimized structures of the reaction intermediates on TiO_2 along CO_2→*CO pathway.

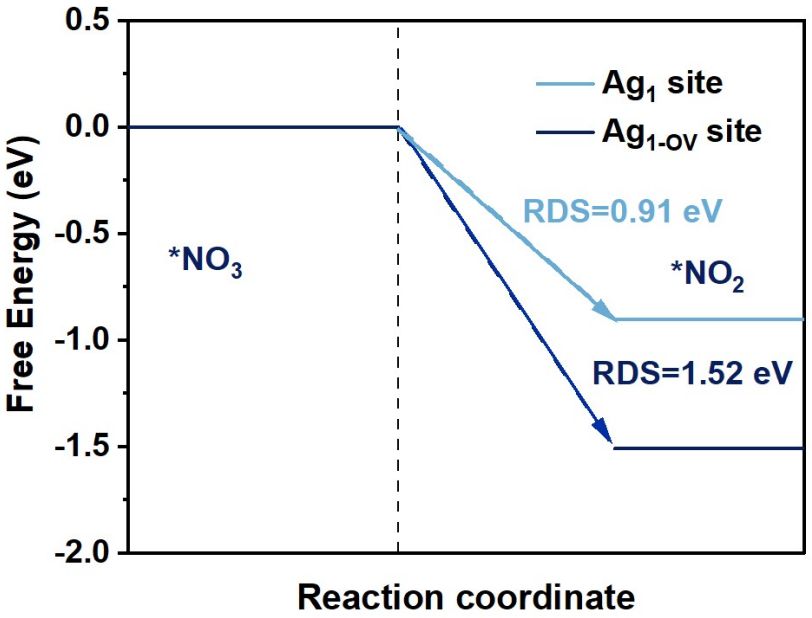

Fig. S28. Free energy diagrams of $*NO_3 \rightarrow *NO_2$ pathways.

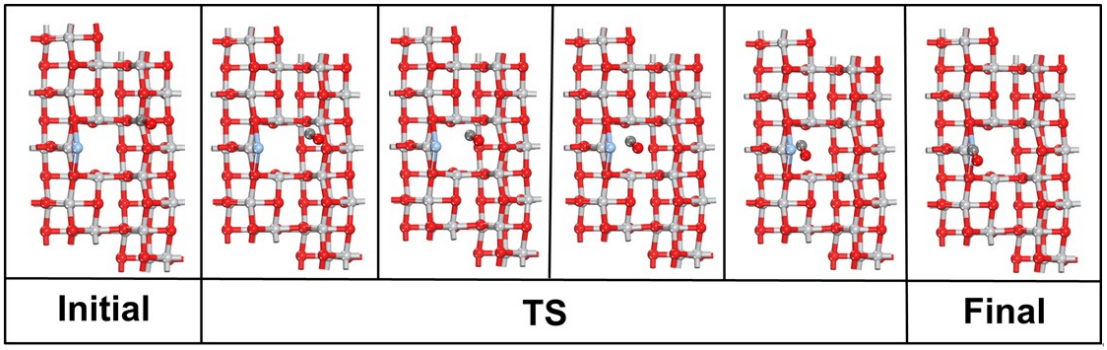

Fig. S29. Optimized structures for the TS calculation of the migration of *CO from Ti_{OV} site to $Ag_{1\text{-}OV}$ site on Ag_1/TiO_{2-x}.

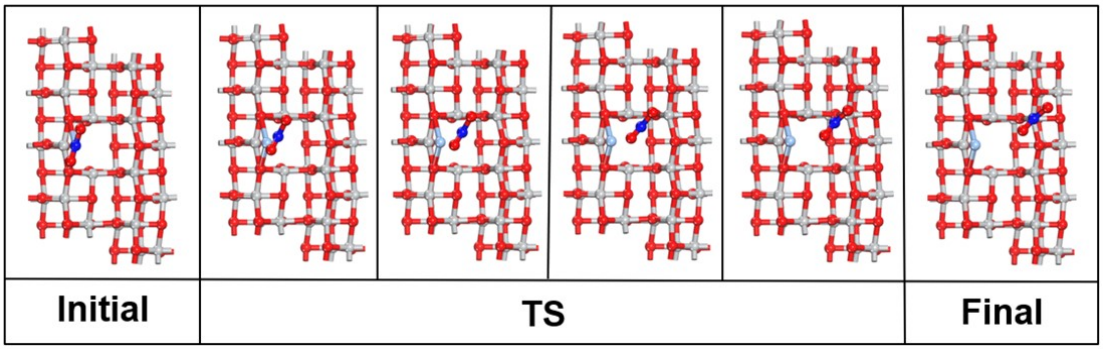

Fig. S30. Optimized structures for the TS calculation of the migration of *NO_2 from $Ag_{1\text{-}OV}$ site to Ti_{OV} site on $Ag_1/TiO_{2\text{-}x}$.

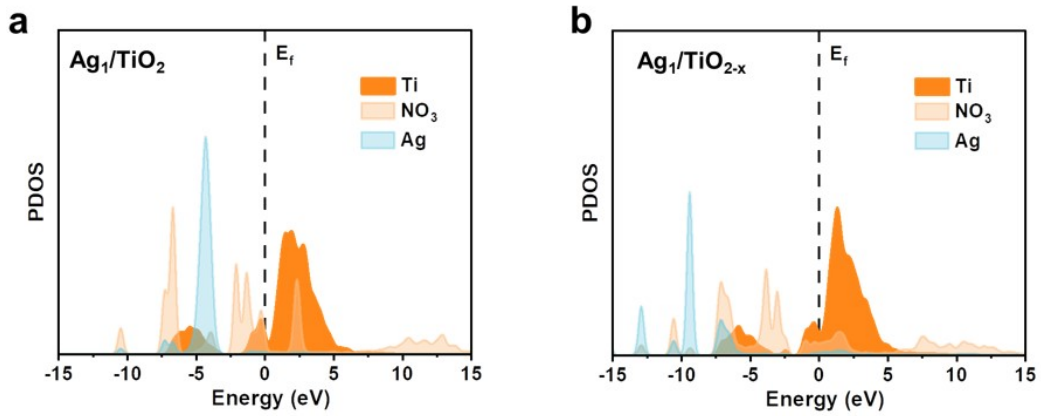

Fig. S31. PDOS profiles of adsorbed NO_3^- on (a) Ag_1/TiO_2 and (b) Ag_1/TiO_{2-x}.

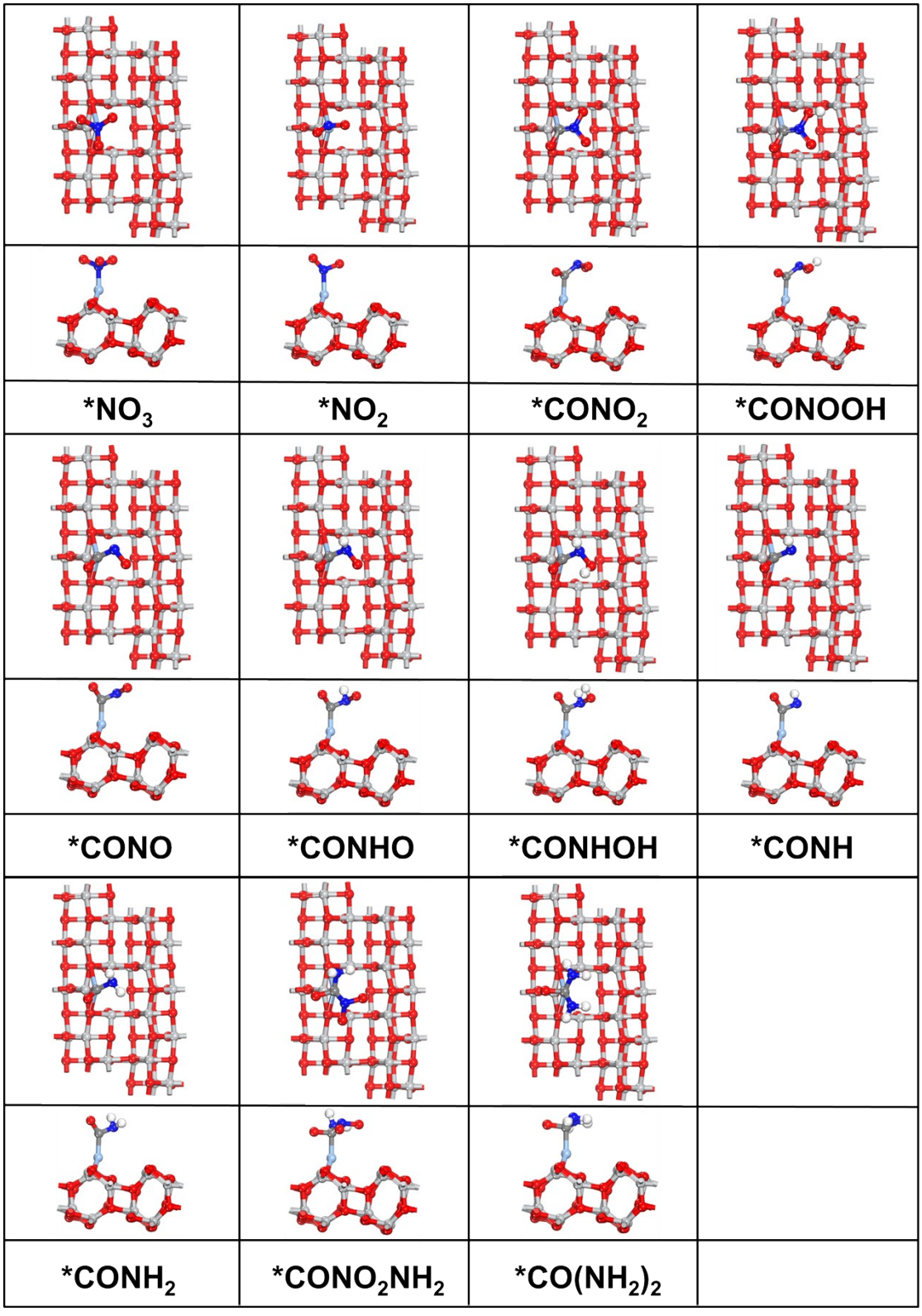

Fig. S32. Optimized structures of the reaction intermediates on Ag_1/TiO_{2-x} along $*NO_3 \rightarrow *CO(NH_2)_2$ pathway.

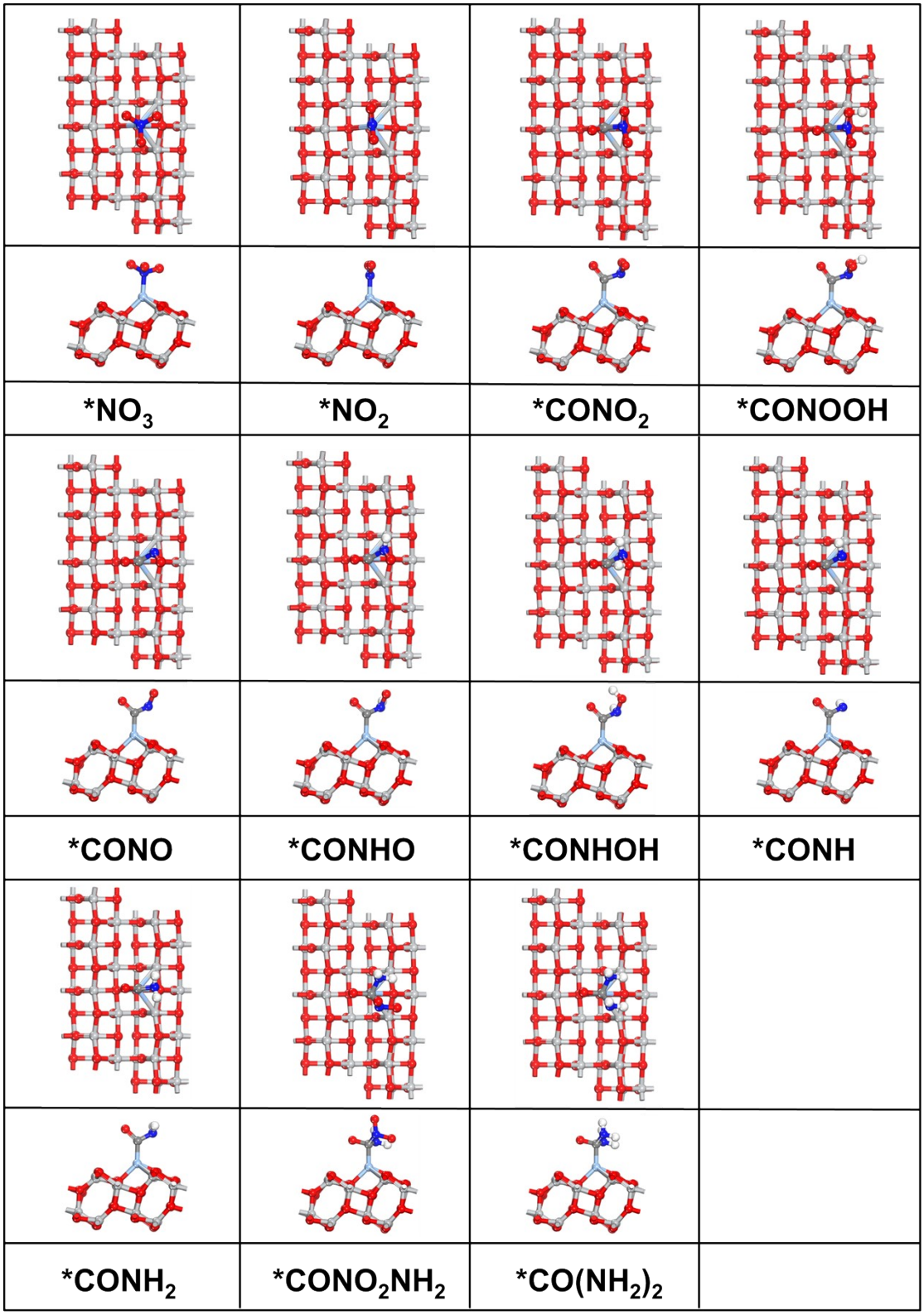

Fig. S33. Optimized structures of the reaction intermediates on Ag_1/TiO_2 along $*NO_3 \rightarrow *CO(NH_2)_2$ pathway.

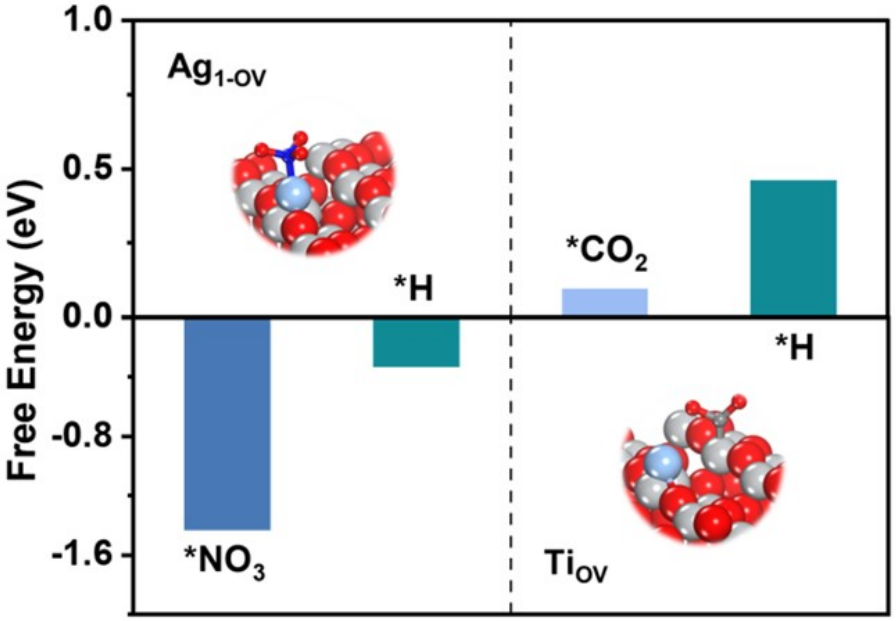

Fig. S34. Binding free energies of $*NO_3$ and *H on $Ag_{1\text{-}OV}$ as well as $*CO_2$ and *H on Ti_{OV} of $Ag_1/TiO_{2\text{-}x}$.

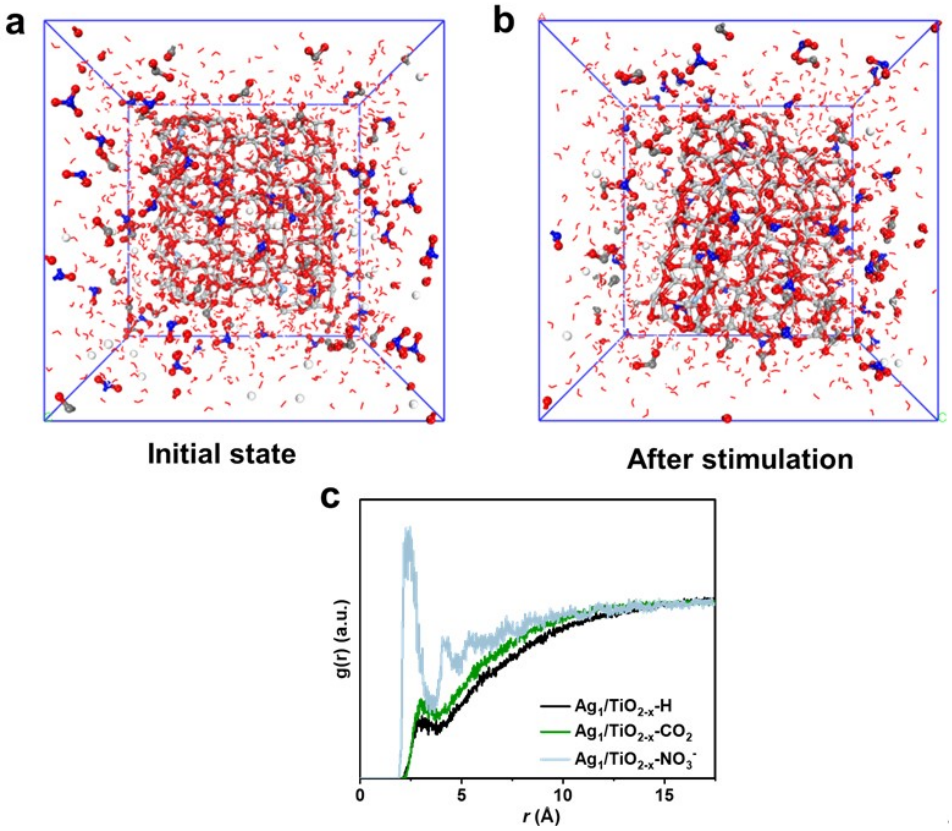

Fig. S35. (a) Initial, (b) final snapshots of the MD simulations of NO_3, CO_2, H_2O and H on Ag_1/TiO_{2-x} and corresponding (c) RDF curves of the interactions between Ag_1/TiO_{2-x} and NO_3^-/CO_2/H.

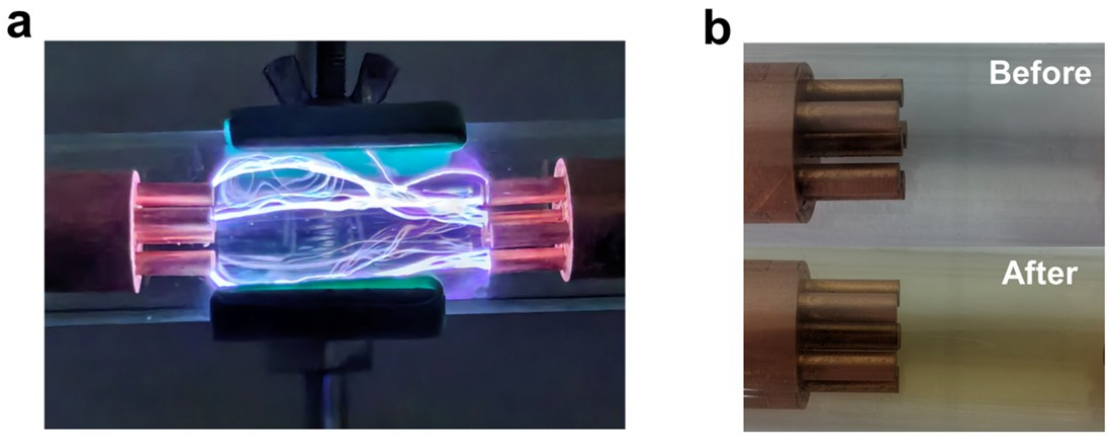

Fig. S36. (a) Photographs for the spark plasma discharge, and (b) corresponding color change in the reaction tube before and after plasma discharge for 10 min.

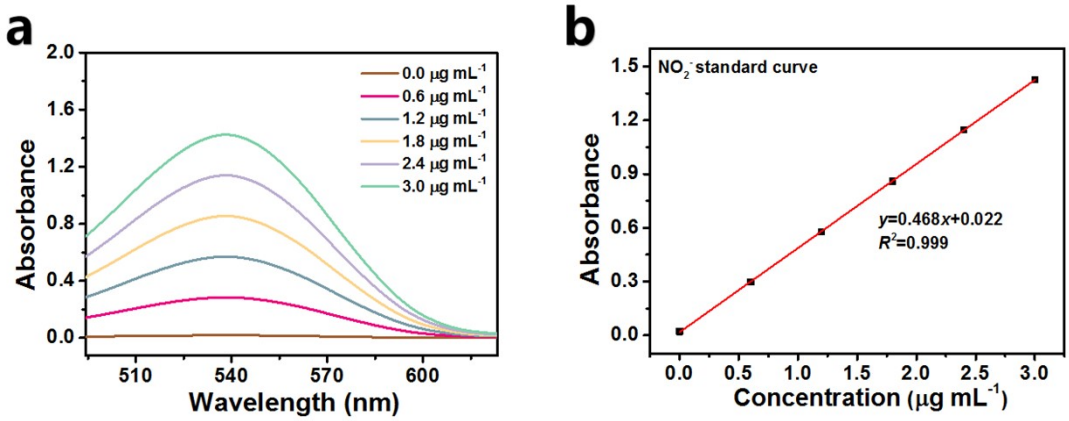

Fig S37. (a) UV-vis absorption spectra of NO_2^- assays after incubated for 20 min at ambient conditions. (b) Calibration curve used for calculation of NO_2^- concentrations.

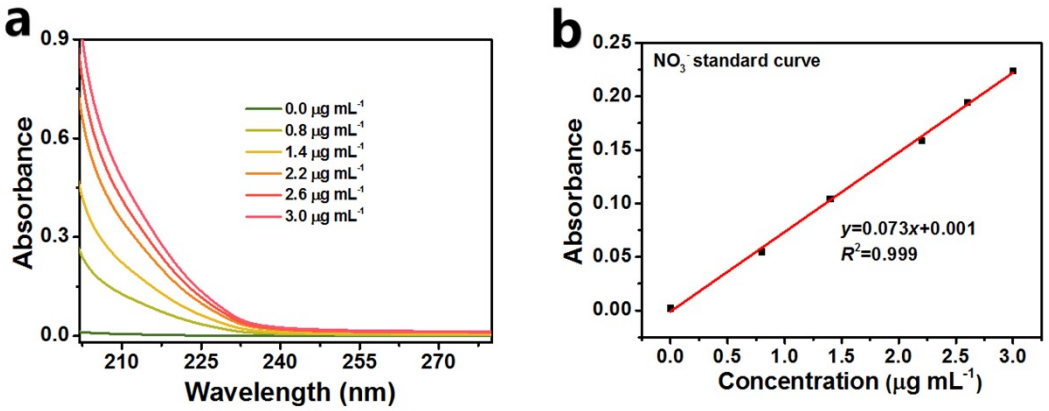

Fig S38. (a) UV-vis absorption spectra of NO_3^- assays after incubated for 20 min at ambient conditions. (b) Calibration curve used for calculation of NO_3^- concentrations.

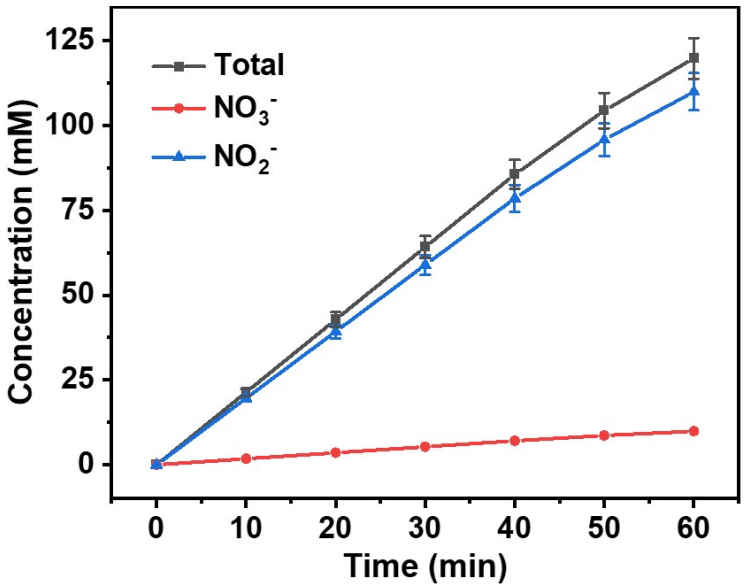

Fig S39.The NO_x^- concentration at different plasma reaction times.

It is seen that prolonged plasma discharge time linearly enhances NO_x^- concentration, with NO_2^- as the dominant species. The persistent NO_2^- selectivity (90.5%-92%) throughout extended operation underscores the effective alkaline (1.0 M KOH) absorption where high OH^- concentration kinetically inhibits NO_2^- oxidation by suppressing the disproportionation reaction.

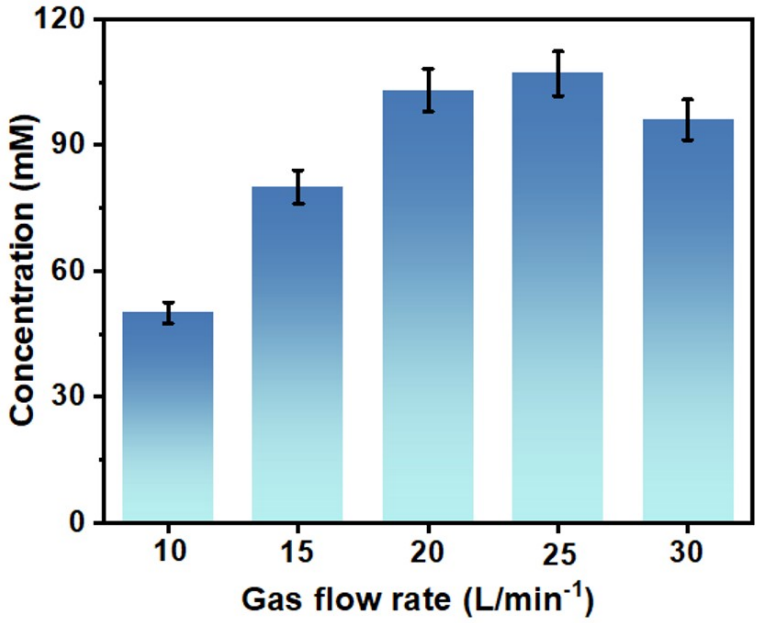

Fig S40. The NO_2^- concentration at different gas flow rates.

It is seen that the air flow rate significantly impacts NO_x^- yield. At 25 L/min, the system achieves peak NO_x^- yield of 118.8 mM after 60 min. This flow rate balances sufficient residence time for radical interactions and effective heat dissipation to prevent NO_2^- degradation. Lower flow rates (<15 L/min) cause overheating and NO_2^- oxidation, while higher flow rates (>25 L/min) reduce radical collisions and NO_x formation efficiency.

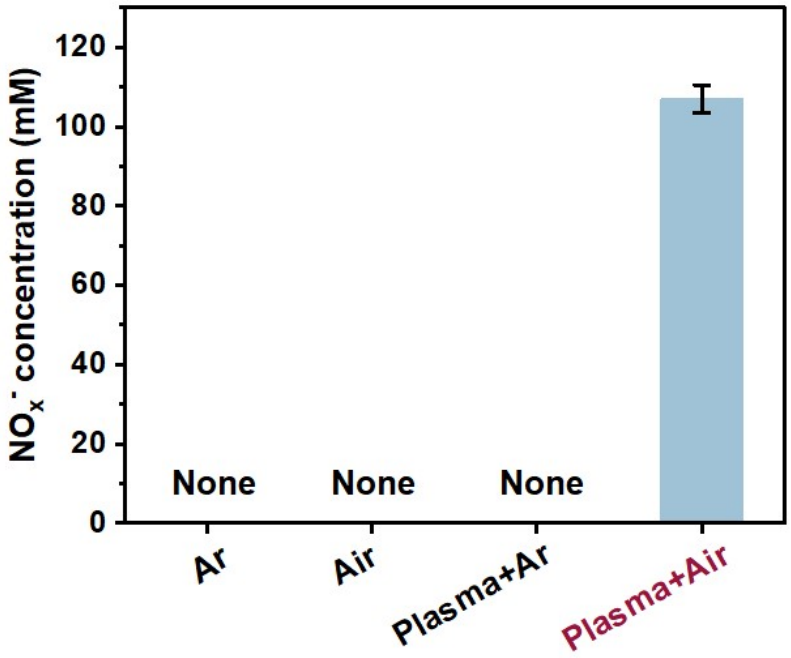

Fig. S41. Amounts of produced NO_x^- on under different conditions.

Control experiments confirm that plasma activation is essential, as NO_x^- is undetectable under Ar-plasma or non-plasma conditions.

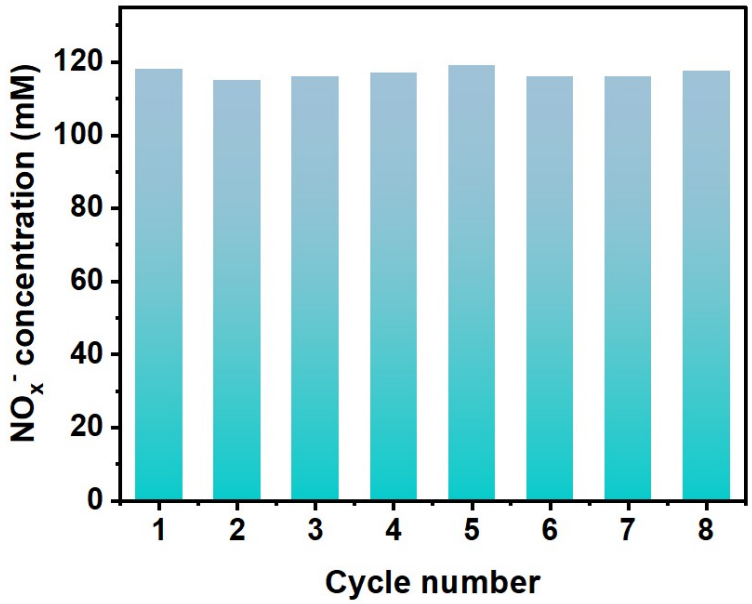

Fig. S42. Cyclic stability tests of plasma-derived NO_x^- production (each cycle for 60 min continuous discharge).

Table S1. Ag K-edge EXAFS fitting results of Ag_1-TiO_{2-x}

Sample	Shell	CN	R (Å)	σ^2 (10^{-3}Å)	$\lvert\Delta E_0\rvert$ (eV)	R factor
Ag_1/TiO_{2-x}	Ag-O	1.9	2.02	5.9	7.8	0.009

CN is the coordination number, R is interatomic distance, σ^2 is Debye-Waller factor, ΔE_0 is edge-energy shift, R factor is used to value the goodness of the fitting.

Table S2. Comparison of the optimum urea yield rate and FE_{urea} for the recently reported state-of-the-art electrocatalysts at ambient conditions.

Catalyst	N/C source	Urea yield rate (mmol $h^{-1}g^{-1}$)	FE_{urea} (%)	Potential (V vs REH)	Ref.
In $(OH)_3$-S	NO_3^- + CO_2	8.88	53.4	-0.6 V	7
Fe(a)@C-Fe_3O_4/CNTs	NO_3^- + CO_2	22.3	16.5	-0.65 V	8
Fe-Ni	NO_3^- + CO_2	20.2	17.8	-1.5 V	9
Vo-CeO_2	NO_3^- + CO_2	15.71	/	-1.6 V	1
F-CNT	NO_3^- + CO_2	6.36	18	-0.65 V	10
m-Cu_2O	NO_3^- + CO_2	29.2	9.43	-1.3 V	11
Vo-InOOH	NO_3^- + CO_2	9.87	51	-0.5 V	12
$CuWO_4$	NO_3^- + CO_2	1.64	70.1	-0.2 V	13
Vo-SIO-6	NO_3^- + CO_2	15.16	60.6	-0.6 V	14
Cu SACs	NO_3^- + CO_2	29.97	28	-0.9 V	15
MoO_X/C	NO_3^- + CO_2	23.83	27.7	-0.6 V	16
Ag_1/TiO_{2-x}	NO_3^- + CO_2	**61.6**	**66.1**	-0.7 V	This work
Ag_1/TiO_{2-x}	**Plasma-derived NO_x^- + CO_2**	**74.6**	**75.7**		

Table S3. Comparison of the NO_x^- yield rate and specific energy consumption for the recently reported state-of-the-art non-thermal plasma.

Plasma discharge system	Feeding gas	Absorption solution	NO_x^- yield rate (mmol h^{-1})	NO_2^- Selectivity (%)	SEC (KW h mol^{-1})	Ref.
Rotating gliding arc plasma jet	Air	0.1 M KOH	9.06	99.34	23.18	17
Double reactor glow and spark discharge with Raschig rings	Air	0.01 M H_2SO_4	2.97	27.03	3.79	18
Dielectric Barrier Discharge	Air	H_2O	0.13	2.44	23.08	19
Jet-type plasma	Air	1 M NaOH	55.29	98.75	11.18	20
spark discharge	Air	H_2O	2.7	--	6.3	21
pulsed high-voltage plasma discharge	Air	1 M NaOH	118.8	90.5	0.857	**This work**

References

1. X. Wei, X. Wen, Y. Liu, C. Chen, C. Xie, D. Wang, M. Qiu, N. He, P. Zhou and W. Chen, *J. Am. Chem. Soc.*, 2022, **144**, 11530-11535.
2. P. Li, Z. Jin, Z. Fang and G. Yu, *Energy Environ. Sci.*, 2021, **14**, 3522-3531.
3. Z.-Y. Wu, M. Karamad, X. Yong, Q. Huang, D. A. Cullen, P. Zhu, C. Xia, Q. Xiao, M. Shakouri and F.-Y. Chen, *Nat. Commun.*, 2021, **12**, 2870.
4. L. C. Green, D. A. Wagner, J. Glogowski, P. L. Skipper, J. S. Wishnok and S. R. Tannenbaum, *Anal. Biochem.*, 1982, **126**, 131-138.
5. Q. Jiang, Z. Ao and Q. Jiang, *Phys. Chem. Chem. Phys.*, 2013, **15**, 10859-10865.
6. X. Li, P. Shen, Y. Luo, Y. Li, Y. Guo, H. Zhang and K. Chu, *Angew. Chem. Int. Ed.*, 2022, **134**, e202205923.
7. C. Lv, L. Zhong, H. Liu, Z. Fang, C. Yan, M. Chen, Y. Kong, C. Lee, D. Liu and S. Li, *Nat. Sustain.*, 2021, **4**, 868-876.
8. J. Geng, S. Ji, M. Jin, C. Zhang, M. Xu, G. Wang, C. Liang and H. Zhang, *Angew. Chem. Int. Ed.*, 2023, **62**, e202210958.
9. X. Zhang, X. Zhu, S. Bo, C. Chen, M. Qiu, X. Wei, N. He, C. Xie, W. Chen and J. Zheng, *Nat. Commun.*, 2022, **13**, 5337.
10. X. Liu, P. V. Kumar, Q. Chen, L. Zhao, F. Ye, X. Ma, D. Liu, X. Chen, L. Dai and C. Hu, *Appl. Catal. B Environ.*, 2022, **316**, 121618.
11. M. Qiu, X. Zhu, S. Bo, K. Cheng, N. He, K. Gu, D. Song, C. Chen, X. Wei and D. Wang, *CCS Chem.*, 2023, **5**, 2617-2627.
12. C. Lv, C. Lee, L. Zhong, H. Liu, J. Liu, L. Yang, C. Yan, W. Yu, H. H. Hng and Z. Qi, *ACS Nano*, 2022, **16**, 8213-8222.
13. Y. Zhao, Y. Ding, W. Li, C. Liu, Y. Li, Z. Zhao, Y. Shan, F. Li, L. Sun and F. Li, *Nat. Commun.*, 2023, **14**, 4491.
14. Z. Li, P. Zhou, M. Zhou, H. Jiang, H. Li, S. Liu, H. Zhang, S. Yang and Z. Zhang, *Appl. Catal. B Environ.*, 2023, **338**, 122962.
15. J. Leverett, T. Tran-Phu, J. A. Yuwono, P. Kumar, C. Kim, Q. Zhai, C. Han, J. Qu, J. Cairney and A. N. Simonov, *Adv. Energy Mater.*, 2022, **12**, 2201500.
16. M. Sun, G. Wu, J. Jiang, Y. Yang, A. Du, L. Dai, X. Mao and Q. Qin, *Angew. Chem.*, 2023, **135**, e202301957.
17. A. Wu, J. Yang, B. Xu, X.-Y. Wu, Y. Wang, X. Lv, Y. Ma, A. Xu, J. Zheng and Q. Tan, *Appl. Catal. B Environ.*, 2021, **299**, 120667.
18. J. Sun, D. Alam, R. Daiyan, H. Masood, T. Zhang, R. Zhou, P. J. Cullen, E. C. Lovell, A. R. Jalili and R. Amal, *Energy Environ. Sci.*, 2021, **14**, 865-872.
19. L. Sivachandiran and A. Khacef, *RSC Adv.*, 2017, **7**, 1822-1832.
20. Z. Meng, J. X. Yao, C. N. Sun, X. Kang, R. Gao, H. R. Li, B. Bi, Y. F. Zhu, J. M. Yan and Q. Jiang, *Adv. Energy Mater.*, 2022, **12**, 2202105.
21. J. Sun, R. Zhou, J. Hong, Y. Gao, Z. Qu, Z. Liu, D. Liu, T. Zhang, R. Zhou and K. K. Ostrikov, *Appl. Catal. B Environ.*, 2024, **342**, 123426.